Hindawi
Advances in Materials Science and Engineering
Volume 2023, Article ID 9785382, 1 page
https://doi.org/10.1155/2023/9785382

Retraction

Retracted: $MoWS_2$ Nanosheet Composite with MXene as Lithium-Sulfur Battery Cathode Material

Advances in Materials Science and Engineering

Received 26 December 2023; Accepted 26 December 2023; Published 29 December 2023

This article has been retracted by Hindawi, as publisher, following an investigation undertaken by the publisher [1]. This investigation has uncovered evidence of systematic manipulation of the publication and peer-review process. We cannot, therefore, vouch for the reliability or integrity of this article.

Please note that this notice is intended solely to alert readers that the peer-review process of this article has been compromised.

Wiley and Hindawi regret that the usual quality checks did not identify these issues before publication and have since put additional measures in place to safeguard research integrity.

We wish to credit our Research Integrity and Research Publishing teams and anonymous and named external researchers and research integrity experts for contributing to this investigation.

The corresponding author, as the representative of all authors, has been given the opportunity to register their agreement or disagreement to this retraction. We have kept a record of any response received.

References

[1] W. Feng, Z. Zhao, Z. Lei, and L. Zhang, "$MoWS_2$ Nanosheet Composite with MXene as Lithium-Sulfur Battery Cathode Material," *Advances in Materials Science and Engineering*, vol. 2023, Article ID 6211780, 10 pages, 2023.

Hindawi
Advances in Materials Science and Engineering
Volume 2023, Article ID 6211780, 10 pages
https://doi.org/10.1155/2023/6211780

Research Article

$MoWS_2$ Nanosheet Composite with MXene as Lithium-Sulfur Battery Cathode Material

Wangjun Feng, Zhiqiang Zhao, Ziru Lei, and Li Zhang

School of Science, Lanzhou University of Technology, Lanzhou 730050, China

Correspondence should be addressed to Wangjun Feng; wjfeng@lut.edu.cn

Received 30 September 2022; Revised 8 October 2022; Accepted 24 November 2022; Published 25 January 2023

Academic Editor: Haichang Zhang

Due to their superior theoretical specific capacity and energy density, lithium-sulfur (L–S) batteries are gaining popularity in order to achieve the growing terms for more power generation. However, drawbacks such as low electrical conductivity of the active ingredient sulfur, severe volume expansion and shuttle effect of polysulfides, rapidly decaying battery capacity, and short battery life have hampered their development. A $MoWS_2$@MXene@CNT composite material is used as the main cathode material for L-S batteries in this study. $MoWS_2$ can improve the electrochemical reaction rate by accelerating polysulfide conversion, whereas MXene can suppress electrode volume expansion. Furthermore, the addition of carbon nanotubes (CNT) with high electrical conductivity improves the rate of the electrochemical reaction. Therefore, the $MoWS_2$@MXene@CNT composites have good capacity and versatility as cathode materials and enhance the behavior of L-S batteries.

1. Introduction

Owing to energy shortages and environmental degradation, the demand for sustainable high-performance electronic devices, such as smartphones and electric vehicles, is increasing [1, 2]. However, commonly used energy storage devices, for instance, lithium-ion batteries, are no longer able to fulfill the growing energy needs of consumers [3–5]. Moreover, lithium-ion batteries for daily use have several disadvantages, such as environmental hazards, high manufacturing costs, and insufficient theoretical capacity [6, 7]. Thus, the exploration of a new generation of energy storage devices is ongoing. In recent years, the development of lithium-sulfur (L-S) batteries has rapidly progressed, positioning them as interchangeable energy materials owing to their environmentally friendliness and inexpensive raw materials [8–10]. However, L-S batteries have disadvantages, such as low electrical conductivity of the active material, shuttle effect of the intermediate product polysulfide, and partial conversion of Li_2S_n ($4 \le n \le 8$) into the last discharge products, thereby limiting their commercialization [11–13].

To overcome these issues, researchers have designed composite materials that can rapidly convert polysulfides and retard the shuttle effect [14, 15]. For example, carbon nanotubes [16], porous carbon [17], and carbon cloths [18] can be used as physical frameworks to accelerate the reaction kinetics and thus mitigate the shuttle effects. Transition metal oxides [19], sulfides [20], and carbides [21] can be used to accelerate the conversion of polysulfides. However, the force between polar materials and polar polysulfides is important in inhibiting the shuttle effect [22–24].

Herein, we synthesized $MoWS_2$@MXene@CNT composites. We selected the molybdenum-based metal sulfide $MoWS_2$ as the cathode material in this study [25, 26] because the strong interactions between the polar material $MoWS_2$ and polar polysulfide can significantly suppress the shuttle effect. Because of their excellent electrical conductivity, carbon nanotubes (CNT) were chosen as the carbon material, which aids in accelerating the conversion of polysulfide [27]. Furthermore, the layered structure of the transition metal carbide MXene [28, 29] can limit volume expansion [30, 31] when singlet sulfur is used as the electrode.

2. Materials and Methods

2.1. Synthesis of $MoWS_2$. First, $Na_2MoO_4{\cdot}2H_2O$ and $Na_2WO_4{\cdot}2H_2O$ in a molar mass ratio of 4 : 1 were dissolved in approximately 40 mL of deionized water. To this mixture, CH_4N_2S and $C_2H_2O_4{\cdot}2H_2O$ in a molar mass ratio of 5 : 1 were subsequently added. As the precursor solution transformed into a clear liquid, it was transferred to a Teflon reactor at 200°C for 24 hours. The contents were then repeatedly cleaned with distilled water before being vacuum dried.

2.2. Synthesis of $MoWS_2$@CNT. $MoWS_2$@CNT was created using a hydrothermal method as follows: first, 60 ml of deionized water was mixed with $MoWS_2$ and CNT in a mass ratio of 1 : 1. Following ultrasonication, the mixture was transferred to a Teflon reactor and the hydrothermal reaction was allowed to run for 12 hours at 200°C. Finally, the contents were cleaned with distilled water before being vacuum dried.

2.3. Synthesis of MXene and $MoWS_2$@MXene@CNT. First, 20 mL of 40% HF was added to a 100 mL Teflon reactor, followed by 10 minutes of slowly adding 1 g of Ti_3AlC_2. The mixture then continuously reacted at a rate of approximately 500 rpm at 40°C for 8 hours to produce MXene. Following etching, the contents were repeatedly cleaned with distilled water and ethanol to remove impurities until a pH of greater than 6 was achieved and then vacuum dried.

The $MoWS_2$@MXene@CNT composites were similarly synthesized. Specifically, the added CNT was converted into the MXene@CNT complex. The complete procedure is shown in Figure 1.

2.4. Synthesis of $MoWS_2$@CNT/S and $MoWS_2$@MXene@CNT/S. Grinding for 10 minutes combined the sulfur powder with the $MoWS_2$@CNT and $MoWS_2$@MXene@CNT powders in a mass ratio of 7 : 3. For 20 hours, the reaction occurred continuously in a Teflon-lined reactor containing argon gas at a temperature of 155°C. Finally, the compound materials $MoWS_2$@CNT/S and $MoWS_2$@MXene@CNT/S were obtained.

2.5. Materials Characterization. X-ray diffraction (XRD, Bruker D8 Advance, Cu-K radiation) was utilized to ascertain the crystallinity of the samples in the 5°–90° test range. Scanning electron microscopy was applied to examine the dimensions and shape of the samples (SEM, JSM-6700F). The internal structure and element distribution of the material were evaluated utilizing transmission electron microscopy (TEM, JEM-2100F). Multifunctional X-ray photoelectron spectroscopy was used to determine the composition and chemical state of the elements in the materials (XPS, SCALAB250Xi). The sulfur content in the materials was proven using thermogravimetric analysis (TGA) (Perkin Elmer TG47).

2.6. Electrochemical Test. The preprepared electrode sheet was cut into 0.6 cm diameter disks with an average surface sulfur loading of 1.5 mg/cm^2. The average thickness of the cathode was 0.1 nm. The components were then gathered, along with the Celgard 2400 septum, unoxidized lithium sheet cathode, Celgard 2025 button cell cathode housing, and lithium-sulfur cell electrolysis. The rate and long cycle assays were conducted on an electrochemical workstation using just a cell test system (CT2001A) with a test voltage range of 1.7–2.8 V. The tests included cyclic voltammetry (CV) and electrochemical impedance spectroscopy (Corrtest 350). Electrochemical impedance spectroscopy (EIS) was tested with a frequency band of 0.01–100 kHz and a voltage amplitude of 5 mV.

3. Results and Discussion

The preparation flowchart of $MoWS_2$@MXene@CNT composite is depicted in Figure 1. In Figure 2(a), the main characteristic peaks of MXene and MXene@CNT are located at 8.7°, 18.3°, 27.4°, 35.2°, and 60.6°, which correspond to the (002), (004), (006), (008), and (110) crystal planes of MXene [32]. Those of MXene@CNT composites are approximately at 26°, which corresponds to the carbon nanotube's (002) crystal plane. Furthermore, Figure 2(a) shows that the characteristic peaks of MXene are sharp, indicating that MXene has excellent crystallinity. The XRD patterns of $MoWS_2$, $MoWS_2$@CNT, and $MoWS_2$@MXene@CNT composites are shown in Figure 2(b). A diffraction peak at 14.1° can be seen in the figure. The shift of the peak at the (002) crystal plane indicates the result of increased layer spacing when compared to the peaks of MoS_2 and WS_2in the literature (JCPDS card numbers: 75-1539 and 08-0237) [25].

Both the $MoWS_2$@CNT and $MoWS_2$@MXene@CNT composites show a minimal change because their overall crystallinity was inferior to that of the original $MoWS_2$ crystals; moreover, the characteristic peaks of $MoWS_2$ and the standard characteristic peaks of CNT dominate these two samples, which could better accelerate the reaction kinetics. $MoWS_2$ composites show obvious sharp (002) diffraction peaks, indicating that the hydrothermally prepared samples possess a high level of crystallinity. Meanwhile, for the composites, the evident diffraction peaks similarly indicate a higher crystallinity for materials prepared by the hydrothermal method, with standard cards at 14.38° and 14.32°, corresponding to the (002) crystal plane of MoS_2 and WS_2, respectively. By comparison, the diffraction peaks of the synthetic $MoWS_2$ (002) are smaller than the fixed peaks, indicating the presence of strain, stress, and a large layer spacing between layers in the structure [26]. In Figure 2(b), the characteristic peak of MXene is significantly lower, indicating that $MoWS_2$ is successfully modified on the $Ti_3C_2T_x$ surface; furthermore, the peak of (002) shifts to the left, indicating increased layer spacing.

TGA was performed on the composites, and the TGA curves of the $MoWS_2$@CNT/S and $MoWS_2$ @MXene@CNT/S composites are presented in Figure 2(c). Meanwhile, the $MoWS_2$@CNT/S and $MoWS_2$ @MXene@CNT/S materials experience rapid mass loss in the 150–300°C range; this mass

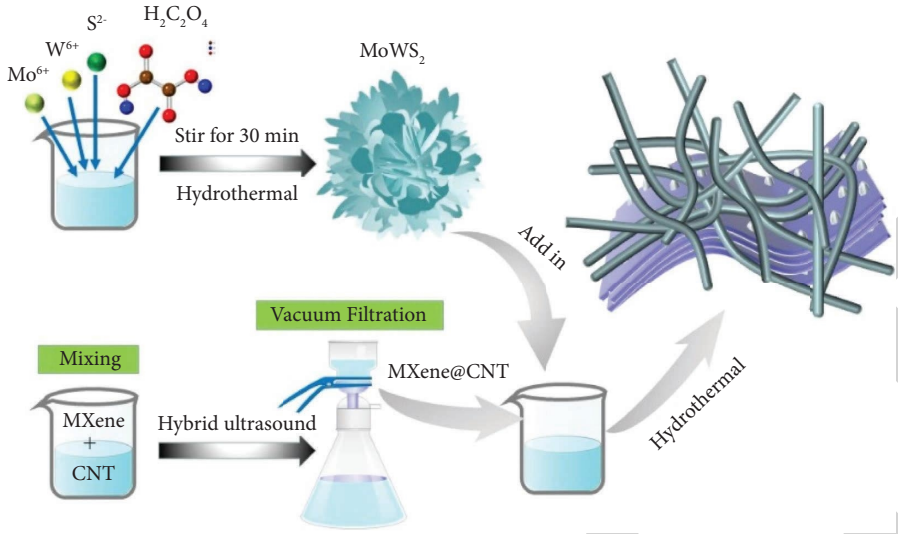

Figure 1: Preparation flowchart of $MoWS_2$@MXene@CNT.

loss is primarily attributed to sulfur sublimation in the composite. The presence of sulfur is confirmed by the presence of a sublimed sulfur diffraction pattern in the material. The mass loss in $MoWS_2$@CNT/S and $MoWS_2$@MXene@CNT/S is 72.63 and 68.73 wt.% sulfur mass fractions, respectively, as shown in Figure 2(c).

After etching of the MAX phase precursor Ti_3AlC_2, the multilayer $Ti_3C_2T_x$ obtained is shown in Figures 3(a)–3(c). The figures show a sparse accordion structure. In Figure 3(d), for the prepared MXene@CNT composites, long strips of CNT are densely compounded on MXene.

In the SEM images of $MoWS_2$ and $MoWS_2$@CNT shown in Figures 3(e), 3(g), and 3(h), the hydrothermally synthesized $MoWS_2$ has a three-dimensional nano-microflower structure and is intertwined in long strips of carbon nanotubes that can provide a good channel for ion transport [25].

For the $MoWS_2$@MXene@CNT composites (Figure 3(i)), the hinged CNT and the nano-microflower $MoWS_2$ are evidently interwoven and born together, and the CNT is densely grown on the surface of MXene. This forms an overall structure with a large and stable specific surface area, which indicates that $MoWS_2$@MXene@CNT was successfully prepared. These morphological and surface analyses confirm that $MoWS_2$@MXene@CNT composites can promote rapid insertion/deinsertion of ions between flowers.

The structure and morphology of the $MoWS_2$@MXene@CNT material were studied using TEM. Many long strips of carbon nanotubes are interwoven with black $MoWS_2$ particles to form a hinge structure (Figure 4(a)) that grow over the MXene to form the $MoWS_2$@MXene@CNT composite material (Figure 4(b)). The (002) lattice plane of CNT is distinctly visible in Figure 4(c).

Figures 5(a) and 5(b) similarly exhibit that the lamellar MXene is interspersed with hinge-like carbon nanotubes and black $MoWS_2$ nanoparticles. Figure 5(c) shows an evident lattice diffraction ring, indicating the good crystallinity of $MoWS_2$@MXene@CNT, which correlates directly to the spacing observed in the XRD plots, and HRTEM analysis confirms the XRD results. All of these results show that $MoWS_2$@MXene@CNT composites can be successfully prepared and have improved electrochemical activity due to their unique structure [25]. The elemental mapping images in Figure 5(d) obtained through the EDX spectroscopy confirm that Ti, C, Mo, S, and W have indeed been successfully coated onto $MoWS_2$@MXene@CNT.

The sample was analyzed by XPS, and the results are shown in Figure 6. The presence of Ti, C, S, Mo, and W in the composites is confirmed by the XPS data.

Figure 6 depicts the composite's entire XPS profile. Figure 6(a) depicts the survey of the underside. The full spectrum shows the peaks of each element, proving that the $MoWS_2$@MXene@CNT composites were synthesized. Figures 6(b)–6(f) show the XPS spectra of Ti, C, Mo, S, and W.

In Figure 6(b), the three major diffraction peaks of Ti 2*p* are observed at 459.6, 465.3, and 469.6 eV, which correspond to the Ti-C (Ti $2p_{3/2}$), Ti-X (Ti $2p_{3/2}$), and TiO_2 (Ti $2p_{3/2}$) bonds, respectively [33].

The C 1*s* spectrum is depicted in Figure 6(c), with three peaks at 284.8, 285.7, and 290.5 eV, corresponding to the C-C/C=C, C-O, and C=O bonds, respectively [34].

In Figure 6(d), two peaks near 162.5 and 163.7 eV, corresponding to S $2p_{3/2}$ and S $2p_{1/2}$, respectively, demonstrate the presence of sulfur in the $MoWS_2$@MXene@CNT composites [35].

The Mo 3*d* spectrum is depicted in Figure 6(e). The Mo 3*d* peak was deconvoluted into two additional peaks at 229.8 and 232.8 eV, corresponding to Mo $3d_{5/2}$ and Mo $3d_{3/2}$, respectively, as well as a S 2*s* peak at 226.7 eV. The Mo 3*d* peak points to the Mo^{4+} [25].

The high-resolution W 4*f* XPS profile of the $MoWS_2$@MXene@CNT samples is displayed in Figure 6(f). The existence of W^{4+} is strongly recommended by the two peaks of W $4f_{7/2}$ and W $4f_{5/2}$ at 37.1 and 39.0 eV, respectively [25, 36].

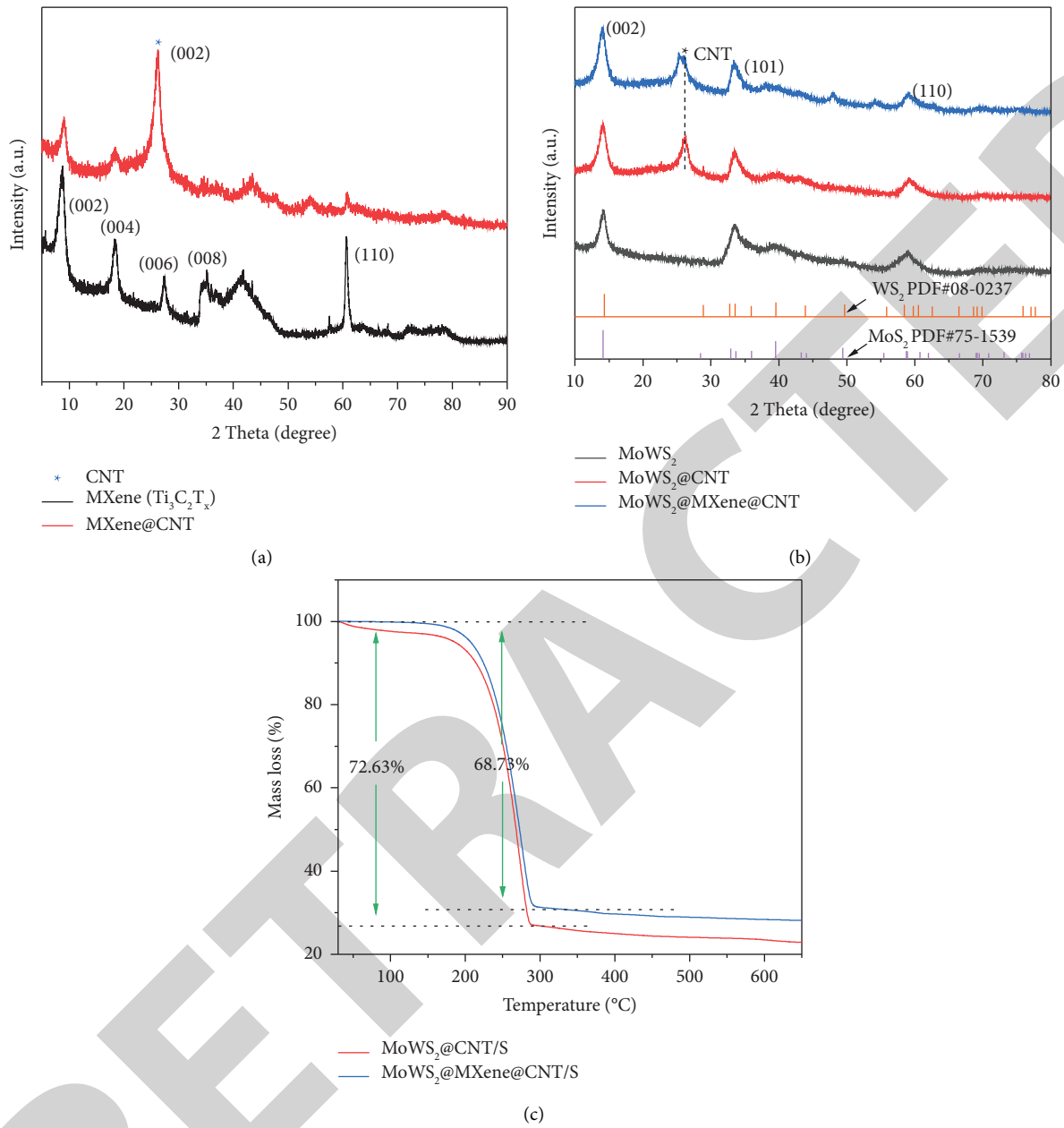

Figure 2: (a) XRD patterns of MXene ($Ti_3C_2T_x$) and MXene@CNT; (b) XRD patterns of $MoWS_2$, $MoWS_2$@CNT, and $MoWS_2$@MXene@CNT; (c) TGA curves of $MoWS_2$@MXene@CNT/S and $MoWS_2$@CNT/S.

The composite was used as the cathode for CR2025 button cell assemblies to evaluate $MoWS_2$@MXene@CNT/S and its electrochemical performance as a cathode material for L-S batteries. The charge/discharge curves, rate performance, and CV diagrams of the $MoWS_2$@MXene@CNT/S and $MoWS_2$@CNT/S composite materials are presented in Figure 7. Figure 7(a) depicts the charge/discharge curve of the $MoWS_2$@MXene@CNT/S. Meanwhile, the discharge profile exhibits a L-S double discharge platform. At approximately 2.3 V, the first plateau is observed, which corresponds to a transition from the elemental sulfur state to the soluble high-valent polysulfides. And the other one is observed at about 2.1 V, corresponding to the transition from Li_2S_n ($4 \le n \le 8$) to Li_2S_2 and Li_2S. Figure 7(b) depicts the composites' rapid loss of discharge capacity as the charging and discharging rates of $MoWS_2$@CNT/S increase. The large capacity loss could be thought to be due to the polysulfide, which ultimately resulted in the continuous loss of active material sulfur as well as the rapid decay of discharge capacity. The discharge capacity of the $MoWS_2$@MXene@CNT/S electrode material is 1319.4 mAh/g, which is clearly superior to that of the $MoWS_2$@CNT/S, which is 996.0 mAh/g. Figure 7(c) shows a rate performance graph of $MoWS_2$@CNT/S and $MoWS_2$@MXene@CNT/S with a discharge rate increasing from 0.1 C to 2 C. The rate performance of $MoWS_2$@MXene@CNT/S electrode is superior to

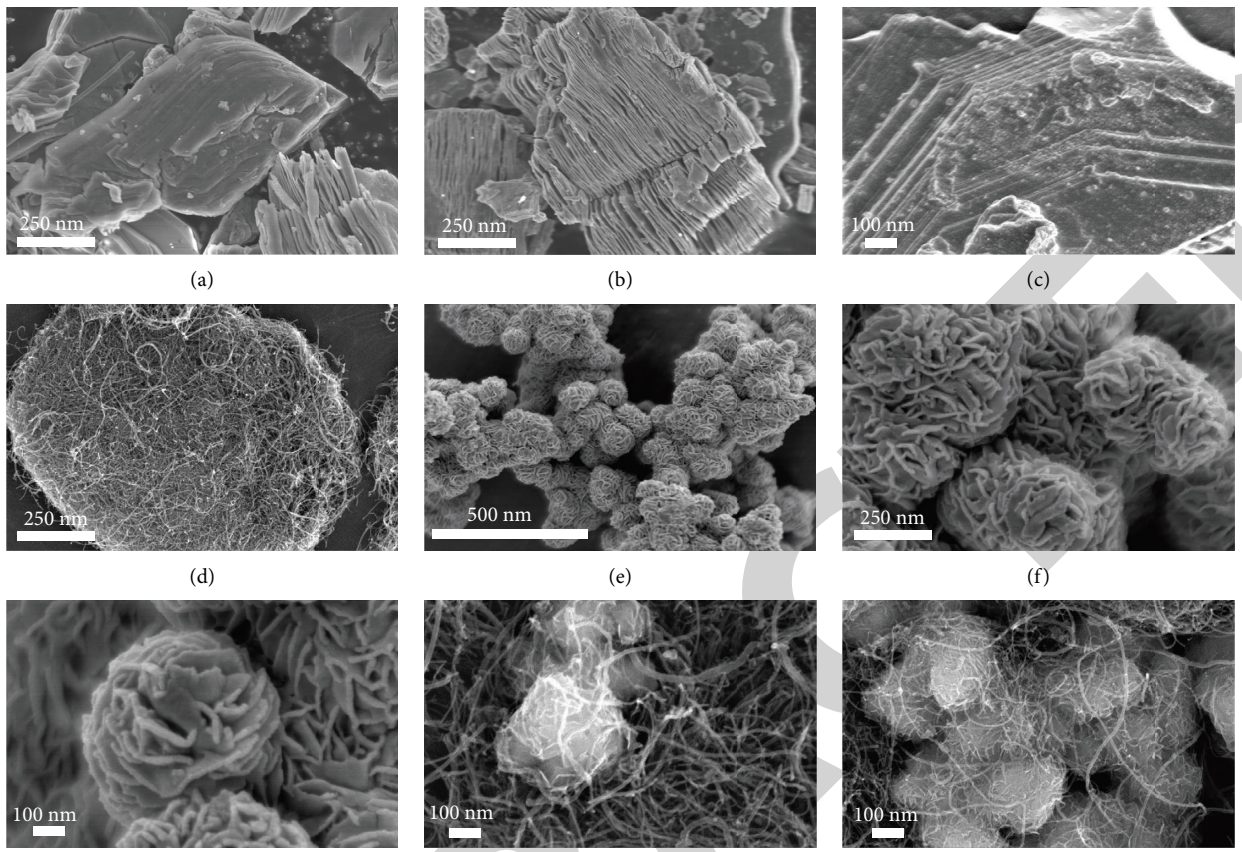

Figure 3: SEM images of (a), (b), and (c) MXene, (d) MXene@CNT, (e), (f), and (g) MoWS2, (h) WS2@CNT, and (i) MoWS2@MXene@CNT.

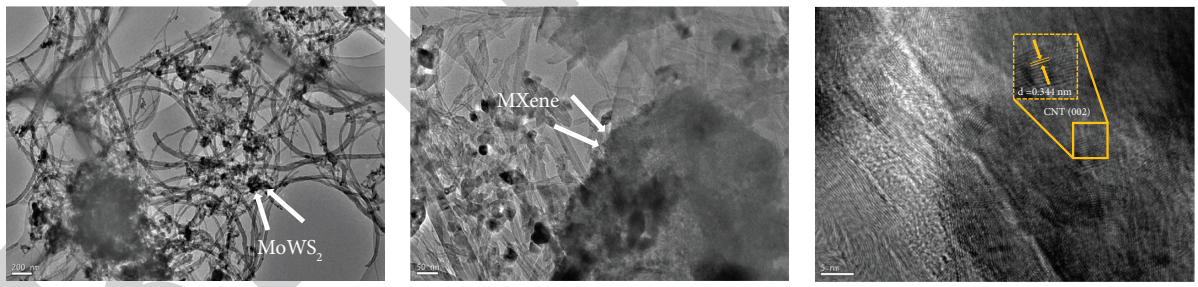

Figure 4: (a) and (b) TEM and (c) HRTEM images of $MoWS_2$@MXene@CNT.

that of $MoWS_2$@CNT/S electrode material. The CV curves were determined to better understand the electrochemical properties of $MoWS_2$@MXene@CNT/S. A split oxidation peak and two reduction peaks are obtained in Figure 7(d). The low and high potential peaks in the reduction peaks are approximately 2.1 and 2.3 V, respectively, corresponding to the insoluble Li_2S_2 and Li_2S and the conversion of the S_8 to high-order polysulfides (Li_2S_n, $4 \le n \le 8$). Because of the occurrence of the reverse reaction from Li_2S to Li_2S_n to S_8 [36], the split oxidation peak is observed at about 2.4 V. Meanwhile, two reduction peaks of $MoWS_2$@MXene@CNT/S have such a greater area than $MoWS_2$@CNT/S, indicating that the addition of MXene can improve polysulfide redox kinetics [37, 38].

The cathode materials $MoWS_2$@MXene@CNT/S and $MoWS_2$@CNT/S have different capacities after 200 cycles at 0.2 C in Figure 8. The $MoWS_2$@MXene@CNT/S cathode material outperforms the $MoWS_2$@CNT/S cathode material in terms of discharge capacity and cycling performance. As a result of electrode material activation, the final capacity of the $MoWS_2$@MXene@CNT/S cathode material slightly increases, which can provide additional lithium interfacial storage at low potentials via a mechanism known as pseudocapacitance [39, 40].

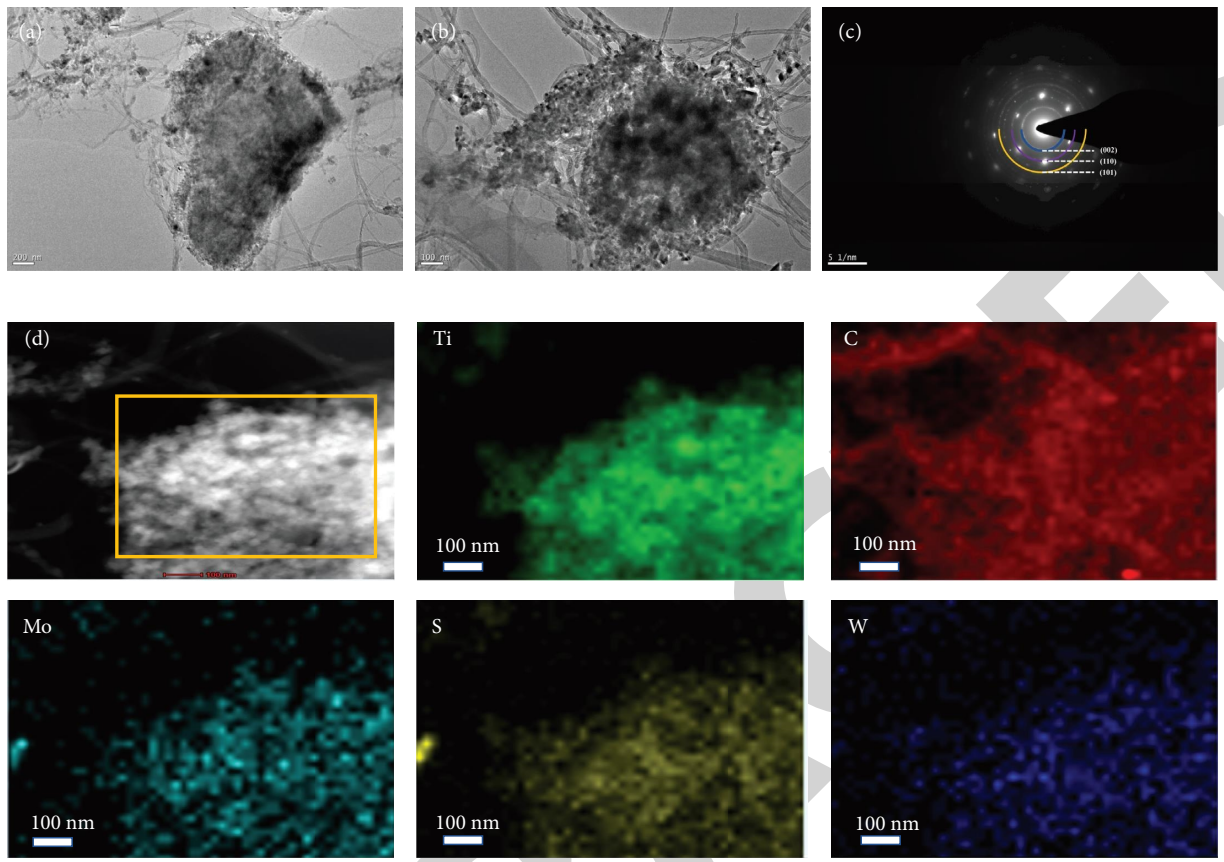

Figure 5: (a) and (b) TEM image of $MoWS_2$@MXene@CNT, (c) SAED pattern of $MoWS_2$@MXene@CNT, and (d) mapping of Ti, C, Mo, S, and W of $MoWS_2$@MXene@CNT.

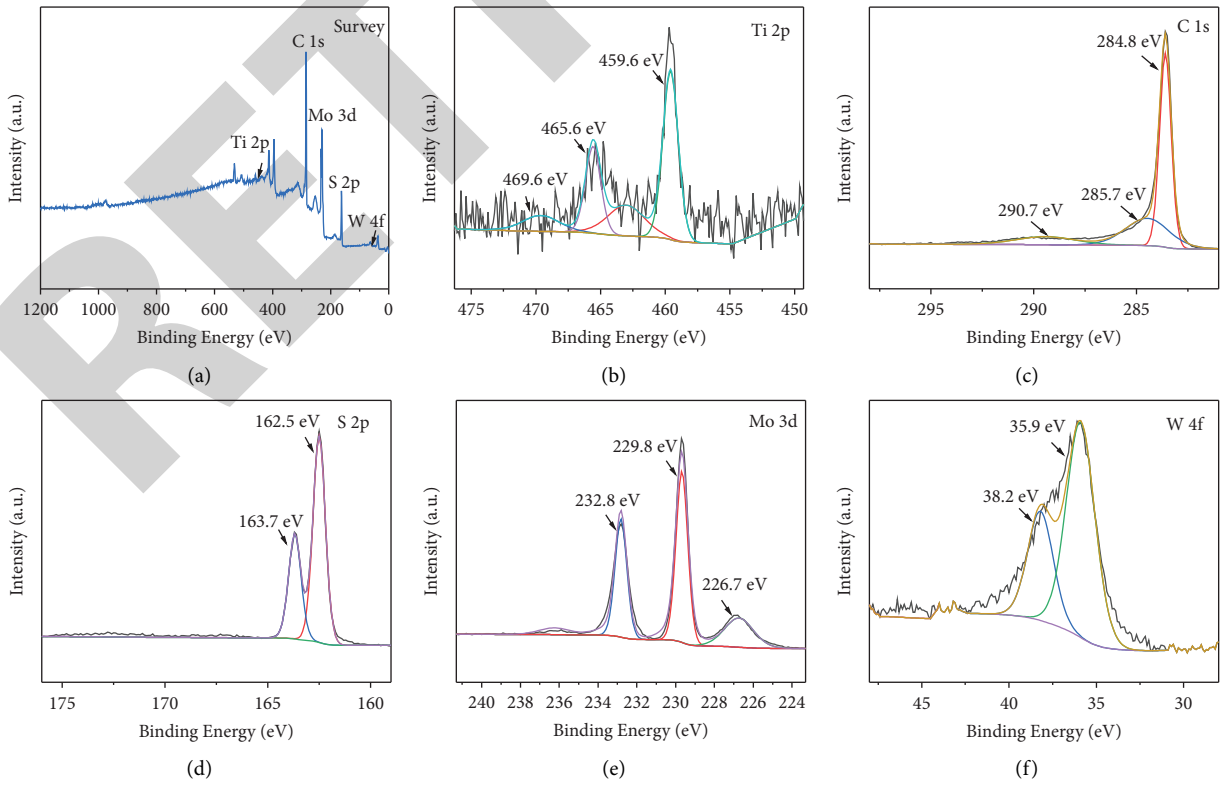

Figure 6: XPS spectra for the $MoWS_2$@MXene@CNT: (a) survey, (b) Ti 2*p*, (c) C 1*s*, (d) S 2*p*, (e) Mo 3*d*, and (f) W 4*f*.

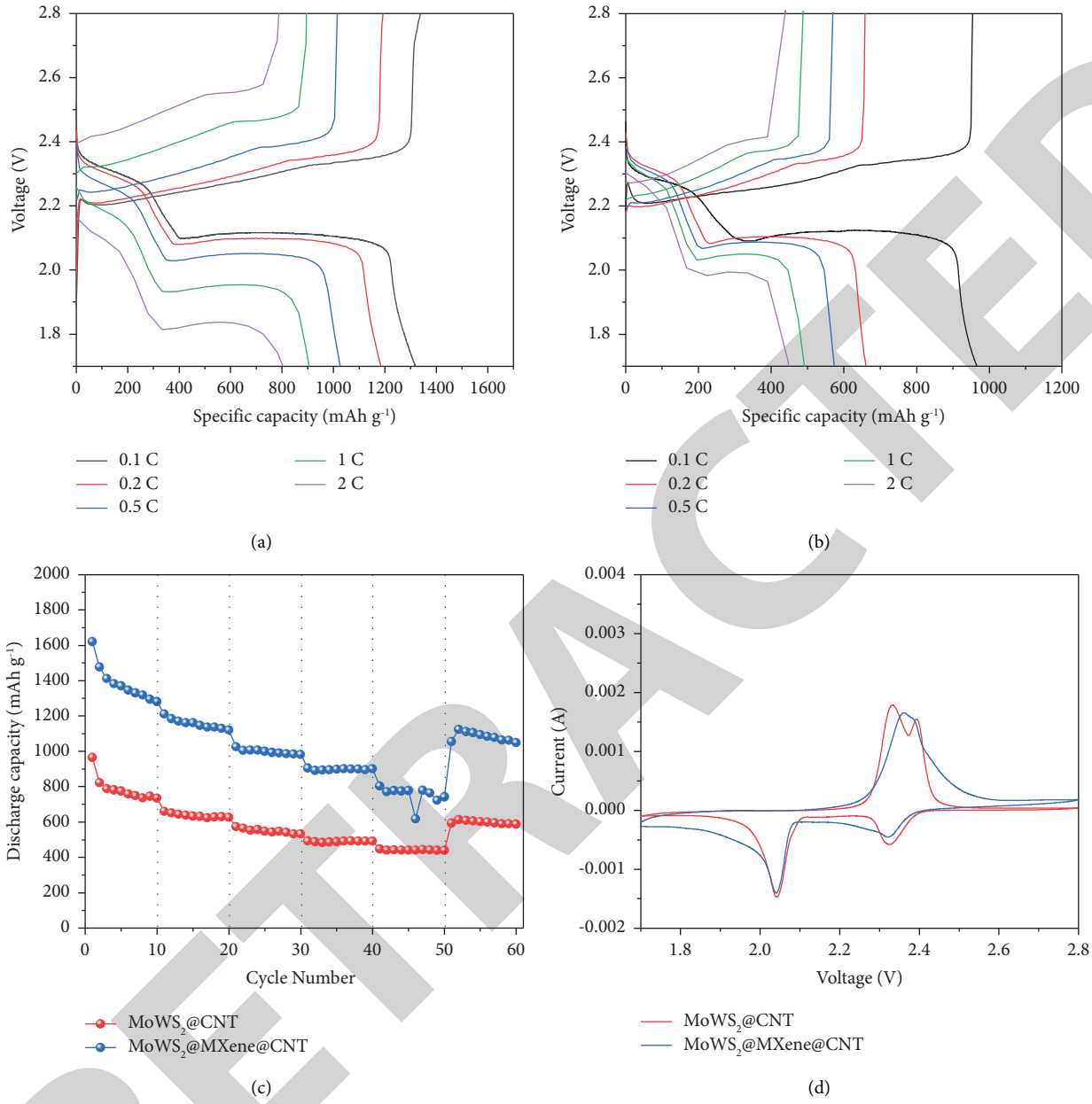

Figure 7: (a) and (b) First charge/discharge profiles of the $MoWS_2$@MXene@CNT/S and the $MoWS_2$@CNT/S, (c) rate curves of the $MoWS_2$@MXene@CNT/S and $MoWS_2$@CNT/S, and (d) C-V curves of the $MoWS_2$@MXene@CNT/S and the $MoWS_2$@CNT/S.

To further evaluate the good electrochemical properties of the $MoWS_2$@MXene@CNT/S composites, the EIS of both electrode materials was investigated separately. In Figure 9, the EIS of both materials have a comparison after and before cycling. A semicircle and a diagonal line comprise the impedance diagram [41, 42]. The semicircle denotes the impedance of charge transfer between the electrode material and the electrolyte, and the diagonal line reflects the diffusion of lithium I in the electrode material [43]. $MoWS_2$@MXene@CNT has the smallest half-circle diameter and total electrochemical resistance before and after the multiplier cycle of the composites, indicating that it has the lowest charge transfer impedance. Table 1 displays the specific fitted values prior to the multiplicative cycle.

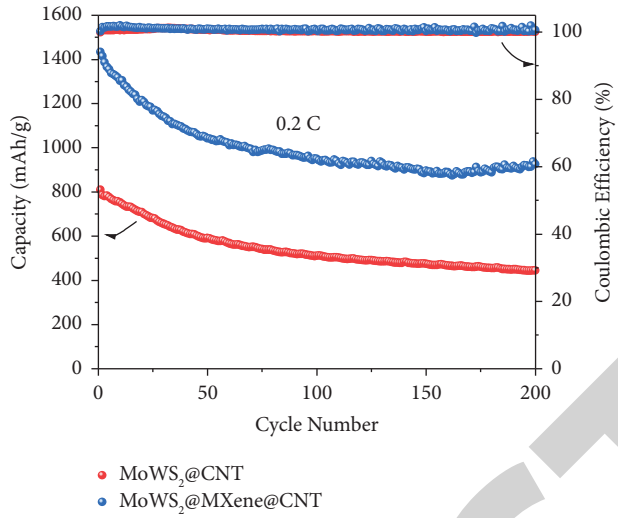

Figure 8: Cycle performance of the $MoWS_2$@MXene@CNT/S and $MoWS_2$@CNT/S cathodes for 200 cycles at 0.2 C.

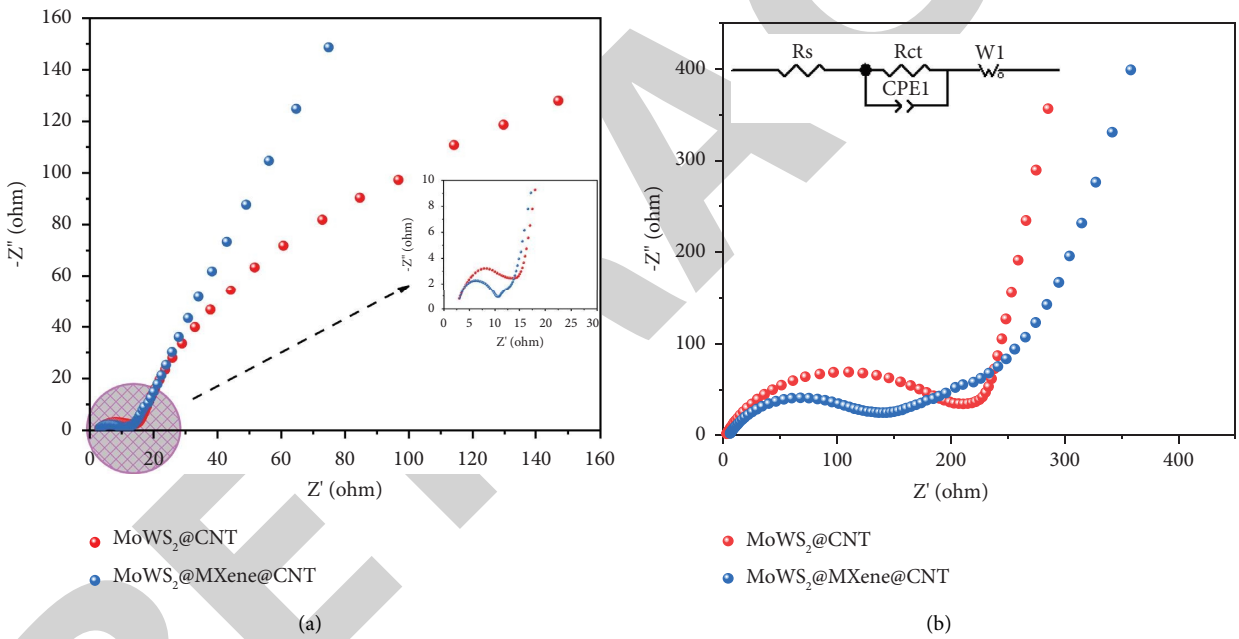

Figure 9: (a) EIS of MoWS2@MXene@CNT/S and MoWS2@CNT/S (a) after and (b) before the multiplication cycle.

Table 1: Composite impedance fitting values (in Ω).

	$MoWS_2$@CNT	$MoWS_2$@MXene@CNT
R_s	2.029	4.405
R_{ct}	188.1	121.8
R_{total}	190.129	126.205

4. Conclusion

In this article, $MoWS_2$, MXene, $MoWS_2$@CNT, and $MoWS_2$@MXene@CNT complexes were prepared by hydrothermal and etching methods. Additionally, the electrode materials after sulfur loading were prepared. These materials were characterized using XRD, TGA, SEM, TEM, and XPS and evaluated for their electrochemical performance. In the $MoWS_2$@MXene@CNT composite, all three substances are simultaneously present in the electrode material. Furthermore, the polar substance $MoWS_2$ can accelerate the conversion of polysulfide, and the highly conductive CNT can accelerate the electron transfer rate. Meanwhile, MXene suppresses the volume expansion of the cell during discharge and enhances the electron conductivity. The final electrochemical tests showed that the $MoWS_2$@MXene@CNT/S electrode material exhibited a good rate and cycling stability compared to the $MoWS_2$@CNT/S electrode material, which provides a reference for transition metal sulfide and

transition metal carbide composites as lithium-sulfur battery cathode materials.

Data Availability

The raw/processed data required to reproduce these findings cannot be shared at this time as the data also form part of an ongoing study.

Conflicts of Interest

The authors declare that they have no conflicts of interest.

Acknowledgments

This work was supported by the National Natural Science Foundation of China (no. 21965019) and HongLiu First-class Disciplines Development Program of Lanzhou University of Technology.

References

[1] C. Li, R. Liu, Y. Xiao, F. Cao, and H. Zhang, "Recent progress of separators in lithium-sulfur batteries," *Energy Storage Materials*, vol. 40, pp. 439–460, 2021.

[2] H. Wang, X. Cao, and W. Liu, "Research progress of the solid state lithium-sulfur batteries," *Frontiers in Energy Research*, vol. 7, p. 112, 2019.

[3] W. Feng, J. Chen, Y. Niu, W. Zhao, and L. Zhang, "CeO_2 composite metal organic framework is used to construct high-performance lithium-sulfur batteries," *Journal of Alloys and Compounds*, vol. 906, Article ID 164341, 2022.

[4] Z. J. Zheng, H. Ye, and Z. P. Guo, "Recent progress on pristine metal/covalent-organic frameworks and their composites for lithium–sulfur batteries," *Energy & Environmental Science*, vol. 14, no. 4, pp. 1835–1853, 2021.

[5] Z. Huang, W. Feng, Z. Lei, W. Li, and W. Zhao, "Effect of ZIF-67 derivative Co_3O_4 on Li-rich Mn-based cathode material $Li_{1.2}Mn_{0.54}Ni_{0.13}Co_{0.13}O_2$," *Ceramics International*, vol. 47, no. 24, pp. 34492–34500, 2021.

[6] Z. Hao, Q. Zhao, J. Tang et al., "Functional separators towards the suppression of lithium dendrites for rechargeable high-energy batteries," *Materials Horizons*, vol. 8, no. 1, pp. 12–32, 2021.

[7] A. Y. S. Eng, V. Kumar, Y. Zhang et al., "Room-temperature sodium–sulfur batteries and beyond: realizing practical high energy systems through anode, cathode, and electrolyte engineering," *Advanced Energy Materials*, vol. 11, no. 14, Article ID 2003493, 2021.

[8] S. Yu, W. Cai, L. Chen, L. Song, and Y. Song, "Recent advances of metal phosphides for Li–S chemistry," *Journal of Energy Chemistry*, vol. 55, pp. 533–548, 2021.

[9] J. Li, Z. Niu, C. Guo, M. Li, and W. Bao, "Catalyzing the polysulfide conversion for promoting lithium sulfur battery performances: a review," *Journal of Energy Chemistry*, vol. 54, pp. 434–451, 2021.

[10] W. Hu, M. Zheng, B. Xu et al., "Design of hollow carbon-based materials derived from metal–organic frameworks for electrocatalysis and electrochemical energy storage," *Journal of Materials Chemistry*, vol. 9, no. 7, pp. 3880–3917, 2021.

[11] Z. Shadike, S. Tan, Q.-C. Wang et al., "Review on organosulfur materials for rechargeable lithium batteries," *Materials Horizons*, vol. 8, no. 2, pp. 471–500, 2021.

[12] J. Ma, Y. Li, N. S. Grundish et al., "The 2021 battery technology roadmap," *Journal of Physics D: Applied Physics*, vol. 54, no. 18, Article ID 183001, 2021.

[13] Y. Li, J. Zhang, Q. Chen, X. Xia, and M. Chen, "Emerging of heterostructure materials in energy storage: a review," *Advanced Materials*, vol. 33, no. 27, Article ID 2100855, 2021.

[14] Z. Tong, L. Huang, W. Lei, H. Zhang, and S. Zhang, "Carbon-containing electrospun nanofibers for lithium–sulfur battery: c," *Journal of Energy Chemistry*, vol. 54, pp. 254–273, 2021.

[15] S. F. Ng, M. Y. L. Lau, and W. J. Ong, "Lithium–sulfur battery cathode design: tailoring metal-based nanostructures for robust polysulfide adsorption and catalytic conversion," *Advanced Materials*, vol. 33, no. 50, Article ID 2008654, 2021.

[16] X. Wang, D. Luo, J. Wang et al., "Strain engineering of a MXene/CNT hierarchical porous hollow microsphere electrocatalyst for a high-efficiency lithium polysulfide conversion process," *Angewandte Chemie International Edition*, vol. 60, no. 5, pp. 2371–2378, 2021.

[17] Z. Zhao, Z. Yi, H. Li et al., "Synergetic effect of spatially separated dual co-catalyst for accelerating multiple conversion reaction in advanced lithium sulfur batteries," *Nano Energy*, vol. 81, Article ID 105621, 2021.

[18] G. Zhou, F. Li, and H.-M. Cheng, "Progress in flexible lithium batteries and future prospects," *Energy and Environmental Science*, vol. 7, no. 4, pp. 1307–1338, 2014.

[19] C. Wang, Y. Yi, H. Li et al., "Rapid gas-assisted exfoliation promises V_2O_5 nanosheets for high performance lithium-sulfur batteries," *Nano Energy*, vol. 67, Article ID 104253, 2020.

[20] S. Nanda, A. Bhargav, and A. Manthiram, "Anode-free, lean-electrolyte lithium-sulfur batteries enabled by tellurium-stabilized lithium deposition," *Joule*, vol. 4, no. 5, pp. 1121–1135, 2020.

[21] D. Xiong, X. Li, Z. Bai, and S. Lu, "Recent advances in layered $Ti_3C_2T_x$ MXene for electrochemical energy storage," *Small*, vol. 14, no. 17, Article ID 1703419, 2018.

[22] Z. Wei, F. Wangjun, S. Zhaojiao, and J Chen, "Enhanced electrochemical performance of MOF-derived nitrogen-enriched porous carbon coated with Ag as the cathode for lithium-sulfur batteries," *Nano*, vol. 16, no. 13, Article ID 2150150, 2021.

[23] J. Chen, X. Wang, W. Feng, W. Zhao, and Z Shi, "Application of ZIF-8 coated with titanium dioxide in cathode material of lithium-sulfur battery," *Journal of Solid State Electrochemistry*, vol. 25, no. 7, pp. 2065–2074, 2021.

[24] J. Chen, W. Feng, W. Zhao, and Z. Shi, "Transition metal phosphide composite with metal-organic framework and carbon nanotubes for high-performance lithium-sulfur batteries," *Journal of Alloys and Compounds*, vol. 890, Article ID 161794, 2022.

[25] A. Patra, M. Shaikh, S. Ghosh, D. J. Late, and C. S. Rout, "$MoWS_2$ nanosheets incorporated nanocarbons for high energy density pseudocapacitive negatrode material and hydrogen evolution reaction," *Sustainable Energy Fuels*, vol. 6, no. 12, pp. 2941–2954, 2022.

[26] D. A. Nguyen, T. S. Le, D. Y. Park, D. Suh, and M. S. Jeong, "Synthesis of $MoWS_2$ on Flexible carbon-based electrodes for high-performance hydrogen evolution eeaction," *ACS Applied Materials & Interfaces*, vol. 11, no. 41, pp. 37550–37558, 2019.

[27] J. Song, M. L. Gordin, T. Xu et al., "Strong lithium polysulfide chemisorption on electroactive sites of nitrogen-doped carbon composites for high-performance lithium-sulfur battery

cathodes," *Angewandte Chemie International Edition*, vol. 54, no. 14, pp. 4325–4329, 2015.

[28] M. Xu, T. Wu, J. Qi, D. Zhou, and Z. Xiao, "V_2C/VO_2 nanoribbon intertwined nanosheet dual heterostructure for highly flexible and robust lithium–sulfur batteries," *Journal of Materials Chemistry*, vol. 9, no. 37, pp. 21429–21439, 2021.

[29] M. Chen, T. Wu, D. Zhou, and Z. Xiao, "Anti-Heterogeneous catalysis revealed by the amidomagnesium halide chemistry in lithium sulfur batteries," *Journal of Catalysis*, vol. 404, pp. 999–1006, 2021.

[30] Y. Tan, M. Yi, Z. Zhu et al., "Carbon-coated $MoSe_2$/MXene heterostructures as active materials for high-performance Na^+ batteries," *Materials Today Communications*, vol. 31, Article ID 103740, 2022.

[31] J. Pang, R. G. Mendes, A. Bachmatiuk et al., "Applications of 2D MXenes in energy conversion and storage systems," *Chemical Society Reviews*, vol. 48, no. 1, pp. 72–133, 2019.

[32] R. Cheng, Z. Wang, C. Cui et al., "One-Step incorporation of nitrogen and vanadium between $Ti_3C_2T_x$ MXene interlayers enhances lithium ion storage capability," *Journal of Physical Chemistry C*, vol. 124, no. 11, pp. 6012–6021, 2020.

[33] C. Shen, L. Wang, A. Zhou et al., "MoS_2-Decorated Ti_3C_2MXene nanosheet as anode material in lithium-ion batteries," *Journal of the Electrochemical Society*, vol. 164, no. 12, pp. A2654–A2659, 2017.

[34] W. Feng, H. Yang, Z. Pu, and L. Zhang, "Study of CNTs-MoS_2/CeO_2 composites for lithium-sulfur battery performance," *Ionics*, vol. 28, no. 6, pp. 2781–2791, 2022.

[35] H. Yang, W. Feng, Z. Pu, J. Chen, W. Zhao, and Z. Huang, "Application of CNTs-MoS_2/SnO_2 p-n heterojunction nanocomposites in lithium-sulfur batteries," *Ferroelectrics*, vol. 596, no. 1, pp. 1–12, 2022.

[36] J. Chen, W. Feng, and W. Zhao, "Anion-doped CeO_2 for high-performance lithium-sulfur batteries," *Applied Surface Science*, vol. 584, Article ID 152613, 2022.

[37] Q. Zhao, Q. Zhu, J. Miao, P. Zhang, and B. Xu, "2D MXene nanosheets enable small-sulfur electrodes to be flexible for lithium–sulfur batteries," *Nanoscale*, vol. 11, no. 17, pp. 8442–8448, 2019.

[38] W. Bao, L. Liu, C. Wang, S. Choi, D. Wang, and G. Wang, "Facile synthesis of crumpled nitrogen-doped MXene nanosheets as a new sulfur host for lithium-sulfur batteries," *Advanced Energy Materials*, vol. 8, no. 13, Article ID 1702485, 2018.

[39] N. Zhang, Q. Zhao, X. Han, J. Yang, and J. Chen, "Pitaya-like Sn@C nanocomposites as high-rate and long-life anode for lithium-ion batteries," *Nanoscale*, vol. 6, no. 5, pp. 2827–2832, 2014.

[40] Y. Lin, L. Sun, J. Wang et al., "RGO wrapped tungsten trioxide hydrate on CNT-modified carbon Cloth as self-supported high-rate lithium-ion battery electrode," *Electrochimica Acta*, vol. 394, Article ID 139162, 2021.

[41] X. Wu, N. Liu, M. Wang et al., "A class of catalysts of BiOX (X = Cl, Br, I) for anchoring polysulfides and accelerating redox reaction in lithium sulfur batteries," *ACS Nano*, vol. 13, no. 11, pp. 13109–13115, 2019.

[42] R. Raccichini, L. Furness, J. W. Dibden, J. R. Owen, and N. Garcia-Araez, "Impedance characterization of the transport properties of electrolytes contained within porous electrodes and separators useful for Li-S batteries," *Journal of the Electrochemical Society*, vol. 165, no. 11, pp. A2741–A2749, 2018.

[43] B. Zhang, C. Luo, G. Zhou et al., "Lamellar MXene composite aerogels with sandwiched carbon nanotubes enable stable lithium–sulfur batteries with a high sulfur loading," *Advanced Functional Materials*, vol. 31, no. 26, Article ID 2100793, 2021.